Quantum Crystal Structure in the 250 K Superconducting Lanthanum Hydride

Ion Errea,[1,2,3] Francesco Belli,[1,2] Lorenzo Monacelli,[4] Antonio Sanna,[5] Takashi Koretsune,[6] Terumasa Tadano,[7] Raffaello Bianco,[2] Matteo Calandra,[8] Ryotaro Arita,[9,10] Francesco Mauri,[4,11] and José A. Flores-Livas *[4]

[1]*Fisika Aplikatua 1 Saila, Gipuzkoako Ingeniaritza Eskola, University of the Basque Country (UPV/EHU), Europa Plaza 1, 20018 Donostia/San Sebastián, Spain*
[2]*Centro de Física de Materiales (CSIC-UPV/EHU), Manuel de Lardizabal Pasealekua 5, 20018 Donostia/San Sebastián, Spain*
[3]*Donostia International Physics Center (DIPC), Manuel de Lardizabal Pasealekua 4, 20018 Donostia/San Sebastián, Spain*
[4]*Dipartimento di Fisica, Università di Roma La Sapienza, Piazzale Aldo Moro 5, I-00185 Roma, Italy*
[5]*Max-Planck Institute of Microstructure Physics, Weinberg 2, 06120 Halle, Germany*
[6]*Department of Physics, Tohoku University, 6-3 Aza-Aoba, Sendai, 980-8578 Japan*
[7]*Research Center for Magnetic and Spintronic Materials, National Institute for Materials Science, Tsukuba 305-0047, Japan*
[8]*Sorbonne Université, CNRS, Institut des Nanosciences de Paris, UMR7588, F-75252, Paris, France*
[9]*Department of Applied Physics, University of Tokyo, 7-3-1 Hongo Bunkyo-ku, Tokyo 113-8656 Japan*
[10]*RIKEN Center for Emergent Matter Science, 2-1 Hirosawa, Wako, 351-0198, Japan*
[11]*Graphene Labs, Fondazione Istituto Italiano di Tecnologia, Via Morego, I-16163 Genova, Italy*
(Dated: February 7, 2020)

The discovery of superconductivity at 200 K in the hydrogen sulfide system at large pressures [1] was a clear demonstration that hydrogen-rich materials can be high-temperature superconductors. The recent predictions of rare earth hydrides with hydrogen cages [2, 3] and the subsequent synthesis of LaH$_{10}$ with a superconducting critical temperature (T$_c$) of 250 K [4, 5] place these materials at the verge of reaching the long-dreamed room-temperature superconductivity. Electrical and x-ray diffraction measurements determined a weakly pressure-dependent T$_c$ for LaH$_{10}$ between 137 and 218 gigapascals in a structure with a face-centered cubic (fcc) arrangement of La atoms [5]. Here we show that quantum atomic fluctuations stabilize in this pressure range a high-symmetry $Fm\bar{3}m$ crystal structure consistent with experiments, which has a colossal electron-phonon coupling of $\lambda \sim 3.5$. Even if *ab initio* classical calculations predict this structure to distort below 230 GPa [2, 3] yielding a complex energy landscape, the inclusion of quantum effects evidences the $Fm\bar{3}m$ as the true ground state. The agreement between the calculated and experimental T$_c$ values further supports this phase as responsible for the 250 K superconductivity. The relevance of quantum fluctuations questions many of the crystal structure predictions made for hydrides within a classical approach that at the moment guide the experimental quest for room-temperature superconductivity [6–8]. Furthermore, quantum effects are revealed to be crucial to stabilize solids with extraordinary λ, which may otherwise be destabilized by the large electron-phonon interaction [9], reducing the pressures needed for their synthesis.

Correspondence and requests for material should be addressed to jose.flores@uniroma1.it

The potential of metallic hydrogen as a high-T$_c$ superconductor [10] was identified few years after the development of the Bardeen-Cooper-Schrieffer (BCS) theory, which explained superconductivity through the electron-phonon coupling mechanism. The main argument was that T$_c$ can be maximized for light compounds due to their high vibrational frequencies. In view of the large pressures needed to metallize hydrogen [11], chemical pre-compression with heavier atoms [12, 13] was suggested as a pathway to decrease the pressure needed to reach metallicity and, thus, superconductivity. These ideas have bloomed into actual realization thanks to modern *ab initio* crystal structure prediction methods based on density-functional theory (DFT) [7, 14, 15]. Hundreds of hydrogen-rich compounds have been predicted to be thermodynamically stable at high pressures and by calculating the electron-phonon interaction, their T$_c$'s have been estimated [6, 7]. The success of this symbiosis between DFT crystal structure predictions and T$_c$ calculations is exemplified by the discovery of superconductivity in H$_3$S at 200 K [1, 16, 17]. The prospects for discovering high-T$_c$ hydrogen-based superconductors in the next years are thus high, especially in rare earth hydrides with sodalite-like clathrate structures [2, 3]. This is in clear contrast with other high-T$_c$ superconducting families such as cuprates or pnictides, where the lack of a clear understanding of the superconducting mechanism hinders an *in silico* guided approach.

DFT predictions in the La-H system proposed LaH$_{10}$ to be thermodynamically stable against decomposition at high pressures [2]. A sodalite type-structure with space group $Fm\bar{3}m$ and T$_c\sim$280 K was suggested above $\sim$220 GPa (see Fig. 1) as a candidate for high-T$_c$ superconductivity [2, 3]. Distorted versions of the $Fm\bar{3}m$ structure with space group $C2/m$ and rhombohedral La sublattice were also discussed [18]. By laser heating a lanthanum sample in a hydrogen-rich atmosphere inside a diamond anvil cell (DAC), a lanthanum superhydride was synthesized [19] right after the first predictions [2, 3].
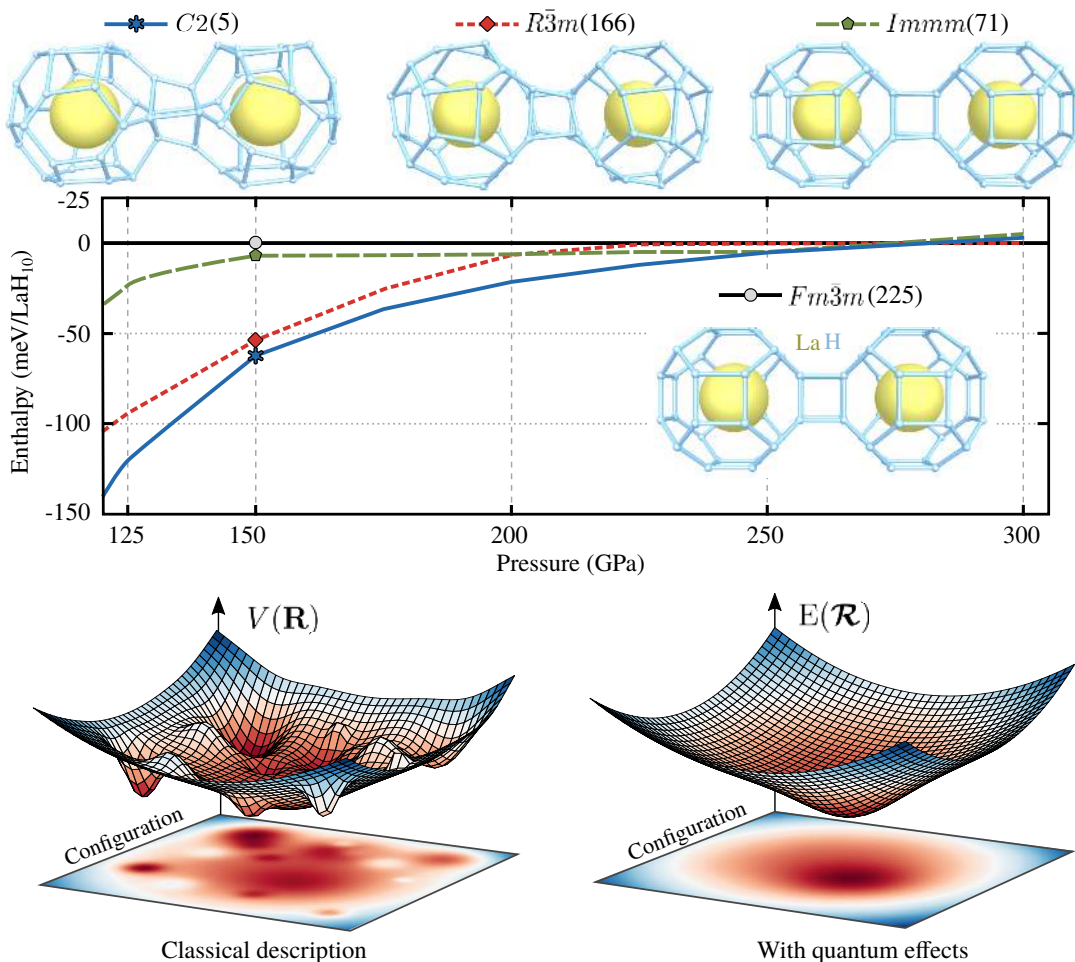
Figure 1. **Quantum effects stabilize the symmetric $Fm\bar{3}m$ phase of LaH$_{10}$.** Top panel: Enthalpy as function of pressure for different structures of LaH$_{10}$ calculated neglecting the zero-point energy. Here pressure is calculated classically from $V(\mathbf{R})$, neglecting quantum effects on it. Bottom left: Sketch of a Born-Oppenheimer energy surface $V(\mathbf{R})$ exemplifying the presence of many local minima belonging to distorted structures. $\mathbf{R}$ represents the positions of atoms treated classically as simple points. Bottom right: sketch of the configurational $E(\boldsymbol{\mathcal{R}})$ energy surface including quantum effects. $\boldsymbol{\mathcal{R}}$ represents the quantum centroid positions, which determine the center of the ionic wave functions, i.e., the average atomic positions. By including quantum effects all phases collapse to a single phase, the highly symmetric $Fm\bar{3}m$.

Based on the unit cell volume obtained by x-ray diffraction, the hydrogen to lanthanum ratio was estimated to be between 9 and 12. An fcc arrangement of the La atoms was determined above ∼160 GPa and a rhombohedral lattice below this pressure with $R\bar{3}m$ space group for the La sublattice. Due to the small x-ray cross section of hydrogen, experimentally it is not possible to resolve directly the H sublattice. Early this year, evidences of a superconducting transition at 260 K and 188 GPa were reported in a lanthanum superhydride [4, 20]. These findings were confirmed and put in solid grounds few months later by an independent group that measured a T$_c$ of 250 K from 137 to 218 GPa in a structure with fcc arrangement of the La atoms and suggested a LaH$_{10}$ stoichiometry [5].

Even if it is tempting to assign the record superconductivity to the $Fm\bar{3}m$ phase predicted previously [2–5],

there is a clear problem: the $Fm\bar{3}m$ structure is predicted to be dynamically unstable in the whole pressure range where a 250 K T$_c$ was observed. This would imply that the phase is not a minimum of the Born-Oppenheimer energy surface. Consequently, no T$_c$ has been estimated for this phase in the experimental pressure range. Considering that quantum proton fluctuations symmetrize hydrogen bonds in the high-pressure X phase of ice [21] and in H$_3$S [22, 23], this contradiction may signal a problem of the classical treatment of the atomic vibrations in the calculations. We show here how quantum atomic fluctuations completely reshape the energy landscape by washing out classical local minima and making the $Fm\bar{3}m$ phase the true ground state and the responsible for the observed superconducting critical temperature.

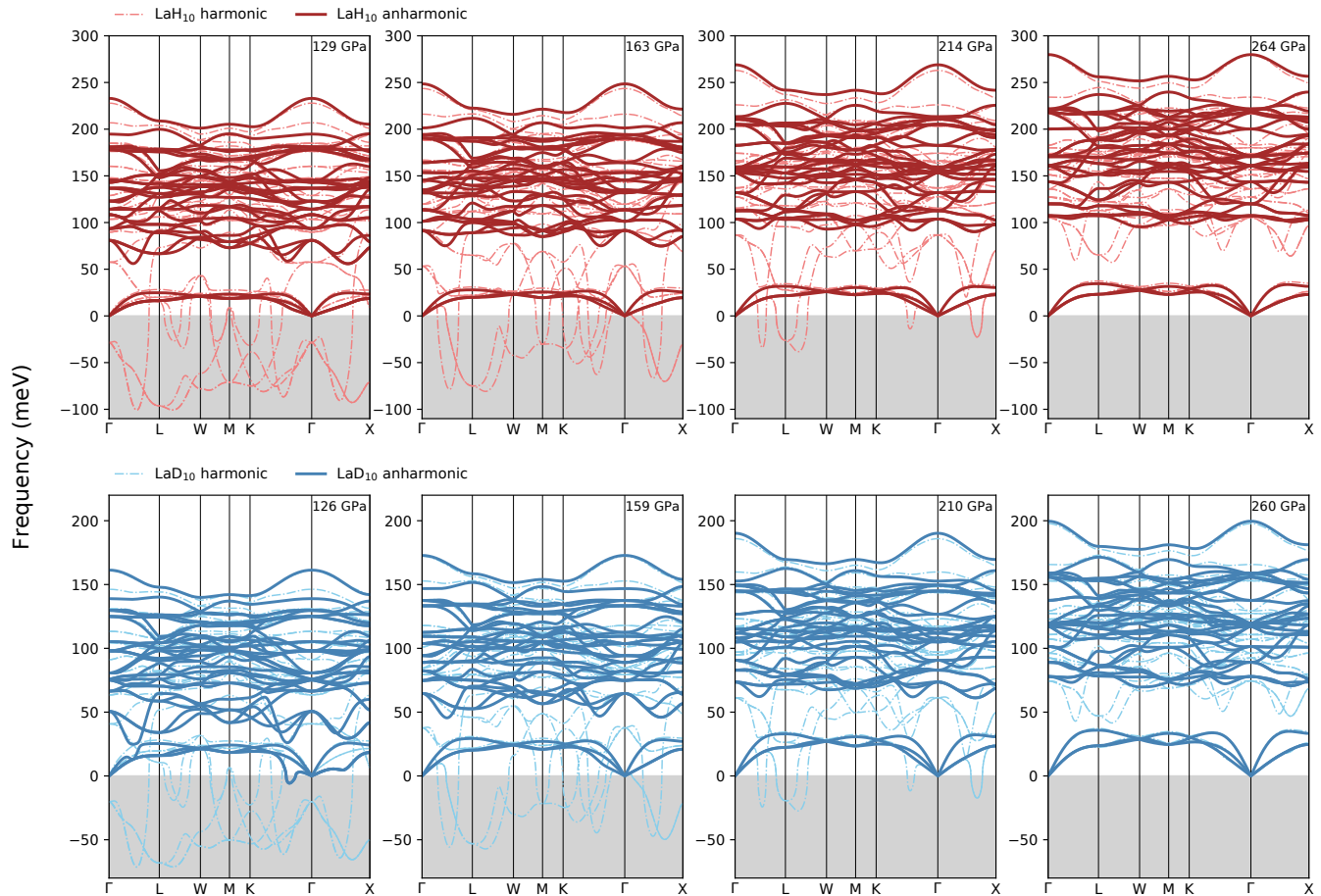We start by calculating using DFT the lowest enthalpy

Figure 2. **Phonon band structure of $Fm\bar{3}m$ LaH$_{10}$ at different pressures.** The harmonic phonons show large instabilities in several regions of the Brillouin zone. Only at the high-pressure limit, e.g. above 220-250 GPa dynamic (harmonic) stabilization is reached. The anharmonic phonons obtained from the Hessian of the quantum $E(\mathcal{R})$ energy within the SSCHA are dynamically stable in the pressure range experimentally relevant. The case of deuterium develops a instability at low pressures (126 GPa) consistent with experimental evidence. The pressure given corresponds to the calculated from $E(\mathcal{R})$ that considers quantum effects. The grey area marks the region with imaginary phonon frequencies, which are depicted as negative frequencies.

structures of LaH$_{10}$ as a function of pressure with state-of-the-art crystal structure prediction methods [24]. The contribution associated with atomic fluctuations is not included, so that the energy just corresponds to the Born-Oppenheimer energy $V(\mathbf{R})$, where $\mathbf{R}$ represents the position of atoms treated classically as simple points. As shown in Figure 1, different distorted phases of LaH$_{10}$ are thermodynamically more stable than the $Fm\bar{3}m$ phase. Above $\sim$250 GPa all phases merge to the $Fm\bar{3}m$ symmetric phase. These results are in agreement with previous calculations [2], even if we identify other possible distorted structures with lower enthalpy such as the $R\bar{3}m$, $C2$ and $P1$ (not shown) phases. These phases not only imply a distortion of the H atoms but also show a La sublattice without an fcc arrangement, and thus should be detectable by x-ray (see Extended Data). The fact that many structures are predicted underlines that the classical $V(\mathbf{R})$ energy surface is of a multifunnel structure tractable to many different saddle and local minima, as

sketched in bottom left of Figure 1.

This picture completely changes when including the energy of quantum atomic fluctuations, the zero-point energy (ZPE). We calculate the ZPE within the stochastic self-consistent harmonic approximation (SSCHA) [25, 26]. The SSCHA is a variational method that calculates the $E(\mathcal{R})$ energy of the system including atomic quantum fluctuations as a function of the *centroid* positions $\mathcal{R}$, which determine the center of the ionic wave functions. The calculations are performed without approximating the $V(\mathbf{R})$ potential, keeping all its anharmonic terms. We perform a minimization of $E(\mathcal{R})$ and determine the centroid positions at its minimum. By calculating the stress tensor from $E(\mathcal{R})$ [26], we relax the lattice parameters seeking for structures with isotropic stress conditions considering quantum effects. We start the quantum relaxation for both $R\bar{3}m$ and $C2$ phases with the lattice that yields a classical isotropic pressure of 150 GPa and vanishing classical forces, i.e. calculated from $V(\mathbf{R})$. All

quantum relaxations quickly evolve into the $Fm\bar{3}m$ phase (see Extended Data). This suggests that the quantum $E(\mathcal{R})$ energy landscape is much simpler than the classical $V(\mathbf{R})$ as sketched in Figure 1. And that the sodalite-type symmetry $Fm\bar{3}m$ phase is the ground state of LaH_{10} in the pressure range of interest. Quantum effects are colossal: reshaping the energy landscape and stabilizing structures by more than 60 meV per LaH_{10}.

Our results further confirm that the structure of LaH_{10} responsible for the 250 K superconductivity is $Fm\bar{3}m$. This is completely consistent with the fcc arrangement of La atoms found experimentally [5]. We verified that the experimental resolution of Ref. [5] is enough to discard the classically obtained distorted structures (see Extended Data). However, Geballe et al. [19] observed a rhombo-hedral distortion below $\sim$160 GPa, with an $R\bar{3}m$ space group for the La sublattice and a rhombohedral angle of approximately 61.3°($c/a \sim 2.38$ in the hexagonal repre-sentation). Our calculations show that this distortion is compatible with the hypothesis of slight anisotropic stress condition, possibly present in some experiments inside the DAC. Indeed, by performing a SSCHA minimization for the $R\bar{3}m$ phase but keeping the rhombohedral angle fixed at 62.3°(the value that yields an isotropic pressure of 150 GPa at the classical level) the quantum stress tensor shows a 6% anisotropy between the diagonal direction and the perpendicular plane. This suggests that anisotropic conditions inside the DAC can produce the $R\bar{3}m$ phase, while it is not ruled out that other experimental stress conditions could favor other crystalline phases.

The $Fm\bar{3}m$ phonon spectra calculated in the harmonic approximation from the Hessian of $V(\mathbf{R})$ show clear phonon instabilities in a broad region of the Brillouin zone (see Figure 2). These instabilities appear below $\sim$230 GPa. This is consistent with the fact that below this pressure many possible atomic distortions lower the enthalpy of this composition. On the contrary, as shown in Figure 2, when calculating the phonons from the Hes-sian of $E(\mathcal{R})$ [25], which effectively captures the full anharmonicity of $V(\mathbf{R})$, no instability is observed. This confirms again that the $Fm\bar{3}m$ phase is a minimum in the quantum-energy landscape in the whole pressure range where a 250 K T_c was observed. While the $Fm\bar{3}m$ phase of LaH_{10} remains a minimum of $E(\mathcal{R})$ as low as $\sim$ 129 GPa, the case of LaD_{10} shows instabilities at 126 GPa, implying that at this pressure the $Fm\bar{3}m$ phase of LaD_{10} distorts to a new phase (as suggested by Drozdov et al. [5]).

The breakdown of the classical harmonic approximation for phonons hinders the estimation of T_c below $\sim$230 GPa in the $Fm\bar{3}m$ phase and questions the certainty of har-monic calculations at higher pressures [2, 27], considering that large anharmonic effects are persistent well above 260 GPa (see Figure 2). On the contrary, with anhar-monic phonons derived from the Hessian of $E(\mathcal{R})$ we can readily calculate the electron-phonon interaction and the superconducting T_c in the experimental range of
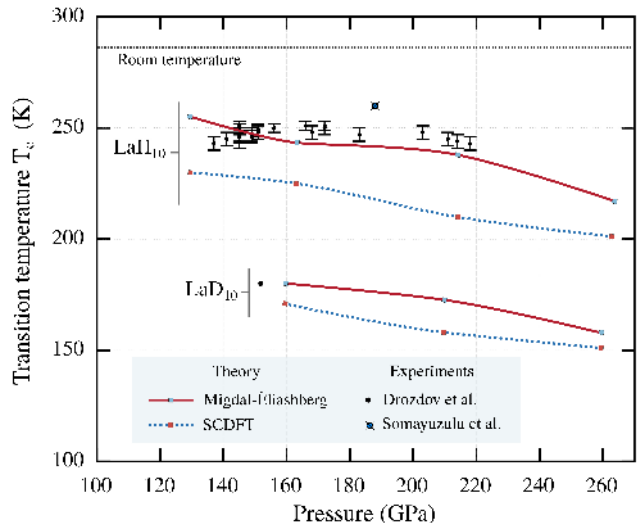

Figure 3. **Summary of experimental and theoretical T_c values.** Superconducting critical temperatures calculated within anisotropic Migdal-Éliashberg equations and SCDFT. In both cases the anharmonic phonons obtained with the SSCHA are used. The results are compared with the experi-mental measurements by Somayuzulu et al. [4] and Drozdov et al. [5]. The error bars in the experimental data by Droz-dov et al. correspond to the experimental uncertainty in the determination of T_c as estimated in this reference.

pressure (137–218 GPa). The superconducting critical temperature is estimated fully *ab initio* –without any empirical parameter– by solving Migdal-Éliashberg (ME) equations and applying SuperConducting DFT (SCDFT). As shown in Figure 3, the numerical solutions of ME equations with anisotropic energy gap are almost on top of the experimental values. SCDFT values systemati-cally show a slightly lower T_c. Our reported values of T_c evidence the phonon-driven mechanism of supercon-ductivity and confirm LaH_{10} in its $Fm\bar{3}m$ structure as responsible for the highest-T_c up to date reported. Our calculations for LaD_{10} in the $Fm\bar{3}m$ phase are also in agreement with the experimental point reported. Despite the large anharmonic effects at play, the isotope coefficient $\alpha = - \left[\ln T_c(LaD_{10}) - \ln T_c(LaH_{10})\right]/\ln 2$ is close to 0.5 (0.43 around 160 GPa), the expected value in BCS theory and is in agreement with the experimentally reported $\alpha = 0.46$.

Finally, we also calculated T_c with the subtle rhombo-hedral distortion that could be induced in experiments by anisotropic stress conditions of pressure. Fixing the rhombohedral angle at 62.3° the obtained T_c for the $R\bar{3}m$ phase at 160 GPa is a 9% lower than for the $Fm\bar{3}m$. Thus, the observed weak pressure dependence of T_c is consistent with the absence of a rhombohedral distortion, as sug-gested by the x-ray data [5]. However, as argued above, undesired anisotropic stress conditions in the DAC can induce phase transitions. It is highly probable that T_c

measurements with lower values around 200 K correspond to distorted structures induced by anisotropic conditions of pressure. In fact, we can safely rule out that compositions such as LaH_{11}, proposed to yield a high critical temperature [5], are responsible for sizable T_c in this range (see Extended Data).

In summary, this work demonstrates how quantum effects are of capital importance in determining the ground state structures of superconducting hydrides, challenging all current predictions and evidencing flaws in standard theoretical methods. Similar effects are expected in other high-T_c compounds with hydrogen clathrate structures claimed to have been synthesized recently [28–30]. More importantly, we illustrated how quantum fluctuations are indispensable to sustain crystals with large λ (λ reaches a record value of 3.6 at 129 GPa for LaH_{10}) that otherwise would be destabilized by the colossal electron-phonon interaction and led to distorted (low symmetry) structures reducing the electronic density of states at the Fermi level (see Extended Data) [9]. Thus, our results give hope for discovering hydrogen-based high-T_c superconductors at much lower pressures than expected classically.

---

[1] A. P. Drozdov, M. I. Eremets, I. A. Troyan, V. Ksenofontov, and S. I. Shylin. Conventional superconductivity at 203 kelvin at high pressures in the sulfur hydride system. *Nature* **525**, 73-76 (2015).

[2] Hanyu Liu, Ivan I. Naumov, Roald Hoffmann, N.W. Ashcroft, and Russell J. Hemley. Potential high-Tc superconducting lanthanum and yttrium hydrides at high pressure. *Proceedings of the National Academy of Sciences* **114**, 6990-6995 (2017).

[3] Feng Peng, Ying Sun, Chris J. Pickard, Richard J. Needs, Qiang Wu, and Yanming Ma. Hydrogen clathrate structures in rare earth hydrides at high pressures: Possible route to room-temperature superconductivity. *Phys. Rev. Lett.* **119**, 107001 (2017).

[4] Maddury Somayazulu, Muhtar Ahart, Ajay K. Mishra, Zachary M. Geballe, Maria Baldini, Yue Meng, Viktor V. Struzhkin, and Russell J. Hemley. Evidence for superconductivity above 260 K in lanthanum superhydride at megabar pressures. *Phys. Rev. Lett.* **122**, 027001 (2019).

[5] A. P. Drozdov, P. P. Kong, V. S. Minkov, S. P. Besedin, M. A. Kuzovnikov, S. Mozaffari, L. Balicas, F. F. Balakirev, D. E. Graf, V. B. Prakapenka, E. Greenberg, D. A. Knyazev, M. Tkacz, and M. I. Eremets. Superconductivity at 250 K in lanthanum hydride under high pressures. *Nature* **569**, 528-531 (2019).

[6] Tiange Bi, Niloofar Zarifi, Tyson Terpstra, and Eva Zurek. The search for superconductivity in high pressure hydrides. *arXiv preprint arXiv:1806.00163* (2018).

[7] José A. Flores-Livas, Lilia Boeri, Antonio Sanna, Gianni Profeta, Ryotaro Arita, and Mikhail Eremets. A Perspective on Conventional High-Temperature Superconductors at High Pressure: Methods and Materials. *arXiv e-prints*, page arXiv:1905.06693 (2019).

[8] Chris J. Pickard, Ion Errea, and Mikhail I. Eremets. Superconducting Hydrides Under Pressure. *Annual Review of Condensed Matter Physics* **11**, doi.org/10.1146/annurev-conmatphys-031218-013413 (2020).

[9] Philip B. Allen and Marvin L. Cohen. Superconductivity and Phonon Softening. *Phys. Rev. Lett.* **29**, 1593 (1972).

[10] N. Ashcroft. Metallic hydrogen: A high-temperature superconductor? *Phys. Rev. Lett.* **21**, 1748 (1968).

[11] Ranga P. Dias and Isaac F. Silvera. Observation of the wigner-huntington transition to metallic hydrogen. *Science* **355**, 715-718 (2017).

[12] J. J. Gilman. Lithium dihydrogen fluoride—an approach to metallic hydrogen. *Phys. Rev. Lett.* **26**, 546 (1971).

[13] N. W. Ashcroft. Hydrogen dominant metallic alloys: High temperature superconductors? *Phys. Rev. Lett.* **92**, 187002 (2004).

[14] Lijun Zhang, Yanchao Wang, Jian Lv, and Yanming Ma. Materials discovery at high pressures. *Nature Reviews Materials* **2**, 17005 (2017).

[15] Artem R. Oganov, Chris J. Pickard, Qiang Zhu, and Richard J. Needs. Structure prediction drives materials discovery. *Nature Reviews Materials* **4**, 331-348 (2019).

[16] Yinwei Li, Jian Hao, Hanyu Liu, Yanling Li, and Yanming Ma. The metallization and superconductivity of dense hydrogen sulfide. *The Journal of Chemical Physics* **140**, 174712 (2014).

[17] Defang Duan, Yunxian Liu, Fubo Tian, Da Li, Xiaoli Huang, Zhonglong Zhao, Hongyu Yu, Bingbing Liu, Wenjing Tian, and Tian Cui. Pressure-induced metallization of dense $(H_2S)_2H_2$ with high-Tc superconductivity. *Sci. Rep.* **4**, 6968 (2014).

[18] Hanyu Liu, Ivan I. Naumov, Zachary M. Geballe, Maddury Somayazulu, John S. Tse, and Russell J. Hemley. Dynamics and superconductivity in compressed lanthanum superhydride. *Phys. Rev. B* **98**, 100102(R) (2018).

[19] Zachary M. Geballe, Hanyu Liu, Ajay K. Mishra, Muhtar Ahart, Maddury Somayazulu, Yue Meng, Maria Baldini, and Russell J. Hemley. Synthesis and stability of lanthanum superhydrides. *Angewandte Chemie International Edition* **57**, 688-692 (2018).

[20] Russell J. Hemley, Muhtar Ahart, Hanyu Liu, and Maddury Somayazulu. Road to Room-Temperature Superconductivity: Tc above 260 K in Lanthanum Superhydride under Pressure. *arXiv e-prints*, page arXiv:1906.03462 (2019).

[21] Magali Benoit, Dominik Marx, and Michele Parrinello. Tunnelling and zero-point motion in high-pressure ice. *Nature* **392**, 258-261 (1998).

[22] Ion Errea, Matteo Calandra, Chris J. Pickard, Joseph R. Nelson, Richard J. Needs, Yinwei Li, Hanyu Liu, Yunwei Zhang, Yanming Ma, and Francesco Mauri. Quantum hydrogen-bond symmetrization in the superconducting hydrogen sulfide system. *Nature* **532**, 81-84 (2016).

[23] Raffaello Bianco, Ion Errea, Matteo Calandra, and Francesco Mauri. High-pressure phase diagram of hydrogen and deuterium sulfides from first principles: Structural and vibrational properties including quantum and anharmonic effects. *Phys. Rev. B* **97**, 214101 (2018).

[24] Stefan Goedecker. Minima hopping: An efficient search method for the global minimum of the potential energy surface of complex molecular systems. *The Journal of Chemical Physics* **120**, 9911 (2004).

[25] Raffaello Bianco, Ion Errea, Lorenzo Paulatto, Matteo Calandra, and Francesco Mauri. Second-order structural phase transitions, free energy curvature, and temperature-

dependent anharmonic phonons in the self-consistent harmonic approximation: Theory and stochastic implementation. *Phys. Rev. B* **96**, 014111 (2017).

[26] Lorenzo Monacelli, Ion Errea, Matteo Calandra, and Francesco Mauri. Pressure and stress tensor of complex anharmonic crystals within the stochastic self-consistent harmonic approximation. *Phys. Rev. B* **98**, 024106 (2018).

[27] Liangliang Liu, Chongze Wang, Seho Yi, Kun Woo Kim, Jaeyong Kim, and Jun-Hyung Cho. Microscopic mechanism of room-temperature superconductivity in compressed LaH_{10}. *Phys. Rev. B* **99**, 140501 (2019).

[28] I. A. Troyan, D. V. Semenok, A. G. Kvashnin, A. G. Ivanova, V. B. Prakapenka, E. Greenberg, A. G. Gavriliuk, I. S. Lyubutin, V. V. Struzhkin, and A. R. Oganov. Synthesis and Superconductivity of Yttrium Hexahydride $Im\bar{3}m$-YH_6. *arXiv e-prints*, page arXiv:1908.01534 (2019).

[29] D. V. Semenok, A. G. Kvashnin, A. G. Ivanova, S. Volodymyr, V. Y. Fominski, A. V. Sadakov, O. A. Sobolevskiy, V. M. Pudalov, I. A. Troyan, and A. R. Oganov. Superconductivity at 161 K in Thorium Hydride ThH_{10}: Synthesis and Properties. *arXiv e-prints*, page arXiv:1902.10206 (2019).

[30] P. P. Kong, V. S. Minkov, M. A. Kuzovnikov, S. P. Besedin, A. P. Drozdov, S. Mozaffari, L. Balicas, F. F. Balakirev, V. B. Prakapenka, E. Greenberg, D. A. Knyazev, and M. I. Eremets Superconductivity up to 243 K in yttrium hydrides under high pressure. *arXiv e-prints*, page arXiv:1909.10482 (2019).

Author contributions. The project was conceived by I.E. and J.A.F.-L. The SSCHA was developed by I.E., L.M., R.B., M.C. and F.M. In particular, R.B. developed the method to compute the quantum energy Hessian and the anharmonic phonon dispersions, and L.M. developed the method to perform a quantum relaxation of the lattice parameters. I.E. and F.B. performed the SSCHA calculations. A.S. T.K., T.T., R.A. and J.A.F.-L. conducted studies on structure prediction and superconductivity. All authors contributed to the editing of the manuscript.

Competing interests. The authors declare no competing interests.

METHODS

Calculation details. First-principles calculations were performed within DFT and the generalized gradient approximation (GGA) as parametrized by Perdew, Burke, and Ernzerhof (PBE) [31]. Harmonic phonon frequencies were calculated within density functional perturbation theory (DFPT) [32] making use of the QUANTUM ESPRESSO code [33, 34]. The SSCHA [25, 26, 35, 36] minimization requires the calculation of energies, forces and stress tensors in supercells. These were calculated as well within DFT at the PBE level with QUANTUM ESPRESSO. For the final SSCHA populations, 1000 configurations were used to reduce the stochastic noise. In all these calculations we used ultrasoft pseudopotentials including 11 electrons for the La atoms, a plane-wave cut-off energy of 50 Ry for the kinetic energy and 500 Ry for the charge density.

In the harmonic phonon calculations for the $Fm\bar{3}m$ and $R\bar{3}m$ phases, we used the primitive and rhombohedral lattices, respectively, with one LaH$_{10}$ formula unit in the unit cell. A $20\times20\times20$ Monkhorst-Pack shifted electron-momentum grid was used for these calculations with a Methfessel-Paxton smearing of 0.02 Ry. The DFT calculations performed for the SSCHA on supercells were performed on a coarser electron-momentum grid, which would correspond to a $12\times12\times12$ grid in the unit cell. We explicitly verified that this coarser mesh yields a fully converged SSCHA gradient with respect to the electron-momentum grid, thus, not affecting the SSCHA minimization. The DFT supercell calculations for the SSCHA minimization on the $C2$ phase were performed keeping the same **k**-point density.

All phonon frequencies for **q**-points not commensurate with the supercell used in the SSCHA minimization were obtained by directly Fourier interpolating the real space force constants obtained in this supercell, which are calculated form the Hessian of $E(\mathcal{R})$. For the $Fm\bar{3}m$ phase the SSCHA calculation was performed both on a $2\times2\times2$ and $3\times3\times3$ supercell containing, respectively, 88 and 297 atoms. The phonon spectra shown in Figure 2 for the $Fm\bar{3}m$ phase are obtained by Fourier interpolating directly the SSCHA energy Hessian force constants obtained in a $3\times3\times3$ supercell. In Extended Data Figure 2 we show that the phonon spectrum obtained interpolating directly the force constants in a $2\times2\times2$ supercell yields similar results, indicating that the energy Hessian force constants are short-range and can be Fourier interpolated. Indeed, the T$_c$ calculated with the $2\times2\times2$ and $3\times3\times3$ force constants for interpolating phonons only differs in approximately 3 K. Upon this, the SSCHA quantum structural relaxations in the $R\bar{3}m$ and $C2$ phases were performed in supercells with 88 atoms.

As shown in Ref. [25], the Hessian of $E(\mathcal{R})$ is

$$\frac{\partial^2 E(\mathcal{R})}{\partial\mathcal{R}\partial\mathcal{R}} = \mathbf{\Phi} + \overset{(3)}{\mathbf{\Phi}}\mathbf{\Lambda}\left[\mathbf{1} - \overset{(4)}{\mathbf{\Phi}}\mathbf{\Lambda}\right]^{-1}\overset{(3)}{\mathbf{\Phi}}. \qquad (1)$$

Bold notation represents matrices and tensors in compact notation. In Eq. (1), $\mathbf{\Phi}$ are the variational force constants of the SSCHA minimization, $\overset{(n)}{\mathbf{\Phi}}$ the quantum statistical averages taken with the SSCHA density matrix of the n-th order derivatives of $V(\mathbf{R})$, and $\mathbf{\Lambda}$ a tensor that depends on the temperature and $\mathbf{\Phi}$. $\mathbf{1}$ is the identity matrix. As we show in Extended Figure 2, setting $\overset{(4)}{\mathbf{\Phi}} = 0$ has a negligible effect on the phonons obtained from the Hessian defined in Eq. (1). Therefore, $\overset{(4)}{\mathbf{\Phi}}$ is neglected throughout, and all superconductivity calculations in the $Fm\bar{3}m$ and $R\bar{3}m$ phases are performed making use of the phonon frequencies and polarization vectors obtained from the Hessian of $E(\mathcal{R})$ with $\overset{(4)}{\mathbf{\Phi}} = 0$. We also estimated T$_c$ with the phonon frequencies and polarization vectors obtained instead from $\mathbf{\Phi}$, resulting in a critical temperature 12 K lower within Allen-Dynes modified McMillan equation. This difference is small and within the uncertainty of the T$_c$ calculation between SCDFT and anisotropic Migdal-Éliashberg calculations (see Figure 3 and below).

The Éliashberg spectral function, which we used for the T$_c$ calculations, is defined as

$$\alpha^2 F(\omega) = \frac{1}{N_{E_F}} \sum_{n\mathbf{k}, m\mathbf{q}, \nu} |g^\nu_{n\mathbf{k}, m\mathbf{k}+\mathbf{q}}|^2 \delta(\epsilon_{n\mathbf{k}} - E_F)$$
$$\times \delta(\epsilon_{m\mathbf{k}+\mathbf{q}} - E_F)\delta(\omega - \omega_{\mathbf{q}\nu}), \qquad (2)$$

where N_{E_F} is the electronic density of states (DOS) at the Fermi energy (E_F), n and m are band indices, **k** is a crystal momentum, $\epsilon_{n\mathbf{k}}$ is a band energy, $\omega_{\mathbf{q}\nu}$ is the phonon frequency of mode ν at wavevector **q**, and $g^\nu_{n\mathbf{k}, m\mathbf{k}+\mathbf{q}}$ is the electron-phonon matrix element between a state $n\mathbf{k}$ and $m\mathbf{k}+\mathbf{q}$. We calculated $\alpha^2 F(\omega)$ combining the SSCHA phonon frequencies and polarization vectors obtained from the Hessian of $E(\mathcal{R})$ with the electron-phonon matrix elements calculated with DFPT. For the $Fm\bar{3}m$ and $R\bar{3}m$ phases, the electron-phonon matrix elements were calculated in a $6\times6\times6$ **q** point grid and a $40\times40\times40$ **k** point grid. These were combined with the SSCHA phonons and polarization vectors obtained by Fourier interpolation to the $6\times6\times6$ **q** point grid from the real space force constants coming from the Hessian of $E(\mathcal{R})$ in a $3\times3\times3$ supercell for the $Fm\bar{3}m$ and in a $2\times2\times2$ supercell for the $R\bar{3}m$. The Dirac deltas on the band energies are estimated by substituting them with a Gaussian of 0.004 Ry width. The calculated $\alpha^2 F(\omega)$ functions for the $Fm\bar{3}m$ phase are shown in Extended Figure 3, while in Extended Figure 5 we show the results for the $R\bar{3}m$ phase.

Crystal phase diagram exploration. To sample the enthalpy landscape of LaH_{10} we employed the minima hopping method (MHM) [24, 37], which has been successfully used for global geometry optimization in a large variety of applications including superconducting materials such as H_3S, PH_3, and elemental solids at high pressure [38–40]. This composition was thoroughly explored with 1, 2, 3 and 4 formula units simulation cells. Variable composition simulations were also performed for other La-H compositions. Energy, atomic forces and stresses were evaluated at the DFT level with the GGA-PBE parametrization to the exchange-correlation functional. A plane wave basis-set with a high cutoff energy of 900 eV was used to expand the wave-function together with the projector augmented wave (PAW) method as implemented in the Vienna Ab Initio Simulation Package VASP [41]. Geometry relaxations were performed with tight convergence criteria such that the forces on the atoms were less than $2\,\mathrm{meV/\AA}$ and the stresses were less than $0.1\;\mathrm{eV/\AA}^3$. Extended Data Figure 1 shows our calculated convex hull of enthalpy formation without considering the zero-point energy at 100, 150 and 200 GPa. Interestingly, there are many stable compositions in the convex hull. LaH_{10} becomes enthalpically stable (classically) at $\sim$175 GPa and remains in the convex well above 300 GPa. We have verified that LaH_{10} ($Fm\bar{3}m$) does not decompose into LaH_3 ($Cmcm$) and LaH_{11} ($P4/nmm$) by $\sim$0.3 eV/LaH_{10} once quantum effects are included in the calculation of the enthalpy formation at 150 GPa, contrary to the conclusion drawn by classical calculations in Ref. [3]. Below 150 GPa, $R\bar{3}m$ and $C2$ phases (LaH_{10}) show unstable harmonic phonon at Γ, becoming saddle points of $V(\mathbf{R})$. However, harmonically one can find $P1$ stable structures (decreasing symmetry) by following the instability pattern (softening direction, i.e. along eigenvector polarization). $P1$ structures are degenerate in enthalpy within less $3\,\mathrm{meV/LaH_{10}}$ with respect $C2$. Hence, we used the $C2$ as a representative of highly distorted structures for our study.

Superconductivity calculations in the $Fm\bar{3}m$ phase. Superconductivity calculations were performed within two different approaches that represent the state-of-the-art of *ab initio* superconductivity: Density functional theory for Superconductors (SCDFT) and the Éliashberg equations with full Coulomb interaction.

SCDFT is an extension to DFT for a superconducting ground state [42, 43]. By assuming that the $n\mathbf{k}$ anisotropy in the electron-phonon coupling is negligible (see Ref. 43 for further details), the critical temperature is computed by solving an (isotropic) equation for the Kohn-Sham gap:

$$\Delta_s(\epsilon) = \mathcal{Z}(\epsilon)\Delta_s(\epsilon) - \int d\epsilon' \mathcal{K}(\epsilon,\epsilon')\frac{\tanh\left[\frac{\beta E(\epsilon')}{2}\right]}{2E(\epsilon')}\Delta_s(\epsilon'),$$

$$(3)$$

where ϵ is the electron energy and β the inverse temperature. The kernels $\mathcal{K}$ and $\mathcal{Z}$ come from the exchange correlation functional of the theory [43–48] and depend on the properties of the pairing interactions: electron-phonon coupling and screened electron-electron repulsion. Eq. 3 allows us to calculate T_c completely *ab initio*, without introducing an empirical μ^* parameter (Coulomb pseudopotential). Dynamic effects on the Coulomb interaction (plasmon) were also tested and did not show any significant effect. In its isotropic form, the screened Coulomb interaction in SCDFT is accounted for by a function $\mu(\epsilon,\epsilon')$, which is given by the average [49] RPA Coulomb matrix element on the iso-energy surfaces ϵ and ϵ' times the DOS at ϵ' ($N(\epsilon')$):

$$\mu(\epsilon,\epsilon') = \sum_{n,m}\iint d^3(kk')V_{n\mathbf{k},m\mathbf{k}'}^{RPA}\frac{\delta(\epsilon-\epsilon_{n\mathbf{k}})}{N(\epsilon_{n\mathbf{k}})}\delta(\epsilon'-\epsilon_{m\mathbf{k}'}).$$

$$(4)$$

The full energy dependence of the DOS is accounted in the calculations, while the electron-phonon coupling is described by the $\alpha^2F(\omega)$ of Eq. (2).

The second approach we use to simulate the superconducting state is the anisotropic Éliashberg approach [50]. Here we include, together with the energy dependence of the electron DOS, the anisotropy of the electron-phonon coupling. The Green's function form of the Éliashberg equation [50] we solve is given as

$$\Sigma_{n\mathbf{k}}(i\omega_i) = -\frac{1}{N\beta}\sum_{\mu,\mathbf{q},m}V_{mn}^{\mathrm{ph}}(\mathbf{q},i\omega_\mu)G_{m\mathbf{k}+\mathbf{q}}(i\omega_\mu+i\omega_i),$$

$$(5)$$

$$\Delta_{n\mathbf{k}}(i\omega_i) = -\frac{1}{N\beta}\sum_{\mu,\mathbf{q},m}\{V_{mn}^{\mathrm{ph}}(\mathbf{q},i\omega_\mu)+V_{mn}^{\mathrm{C}}(\mathbf{q},i\omega_\mu)\}$$
$$\times |G_{m\mathbf{k}+\mathbf{q}}(i\omega_\mu+i\omega_i)|^2\Delta_{m\mathbf{k}+\mathbf{q}}(i\omega_\mu+i\omega_i). \quad (6)$$

Here, $\Sigma_{n\mathbf{k}}(i\omega_i)$ and $\Delta_{n\mathbf{k}}(i\omega_i)$ are the normal and anomalous self energy, and $V_{mn}^{\mathrm{ph}}(\mathbf{q},i\omega_\mu)$ and $V_{mn}^{\mathrm{C}}(\mathbf{q},i\omega_\mu)$ are the $\mathbf{k}$-averaged phonon-mediated interaction and Coulomb interaction, respectively. The explicit form of $V_{mn}^{\mathrm{ph}}(\mathbf{q},i\omega_\mu)$ is given as

$$V_{mn}^{\mathrm{ph}}(\mathbf{q},i\omega_\mu) = \sum_\nu |g_{nm}^\nu(\mathbf{q})|^2 D_\nu(\mathbf{q},i\omega_\mu), \quad (7)$$

where $|g_{nm}^\nu(\mathbf{q})|^2$ is a $\mathbf{k}$-averaged electron-phonon matrix element,

$$|g_{nm}^\nu(\mathbf{q})|^2 = \frac{\sum_{\mathbf{k}}|g_{n\mathbf{k},m\mathbf{k}+\mathbf{q}}^\nu|^2\delta(\epsilon_{n\mathbf{k}}-E_F)\delta(\epsilon_{m\mathbf{k}+\mathbf{q}}-E_F)}{\sum_{\mathbf{k}}\delta(\epsilon_{n\mathbf{k}}-E_F)\delta(\epsilon_{m\mathbf{k}+\mathbf{q}}-E_F)},$$

$$(8)$$

and $D_\nu(\mathbf{q}, i\omega_\mu)$ is a free-phonon Green's function, $D_\nu(\mathbf{q}, i\omega_\mu) = -2\omega_{\mathbf{q}\nu}/(\omega_\mu^2 + \omega_{\mathbf{q}\nu}^2)$. The electron-phonon matrix elements are calculated through a DFPT calculation with $6\times6\times6$ $\mathbf{q}$ point grid and are combined with the phonon frequencies and polarization vectors obtained by directly Fourier interpolating to this grid the force constants coming from the $E(\mathcal{R})$ Hessian in the $3\times3\times3$ supercell. For the Coulomb interaction, $V_{mn}^{\mathrm{C}}(\mathbf{q}, i\omega_\mu)$ is approximated by $\mathbf{k}$-averaged static Coulomb interaction within the random phase approximation, $\frac{1}{N_k}\sum_{\mathbf{k}} V_{m\mathbf{k},n\mathbf{k}+\mathbf{q}}^{\mathrm{RPA}}(i\omega_\mu = 0)$. Using Eq. (5), the Dyson equation was solved self-consistently and then Eq. (6) was solved to estimate T_c with $36\times 36 \times 36$ $\mathbf{k}$ point grid and 512 Matsubara frequencies.

In Extended Data Table I we summarize all calculated T_c's within anisotropic ME and isotropic SCDFT. We also include the values obtained with McMillan equation and Allen-Dynes modified McMillan equation (μ^*=0.1). The calculated electron-phonon coupling constant, $\lambda = 2\int_0^\infty d\omega \alpha^2 F(\omega)/\omega$, and the logarithmic frequency average, $\omega_{log} = \exp\left(\frac{2}{\lambda}\int_0^\infty d\omega \frac{\alpha^2 F(\omega)}{\omega}\log\omega\right)$, are also included in the table.

Quantum structural relaxations in the $R\bar{3}m$ and $C2$ phases. In Extended Figure 5 we show the evolution of the pressure calculated along the different Cartesian directions for the $R\bar{3}m$ throughout the SSCHA minimization but keeping the rhombohedral angle fixed at 62.3°. Thus, the centroid positions $\mathcal{R}$ are optimized only considering the internal degrees of freedom of the $R\bar{3}m$ phase. Even if at the classical level the stress is isotropic (within a 0.5%), after the SSCHA quantum relaxation an anisotropic stress of a 6% is created between the z and $x-y$ directions. The phonons obtained at the end of the minimization are shown in Extended Figure 5. Secondly, in Extended Figure 4, we show that starting from the result of this minimization but now relaxing also the lattice, the $R\bar{3}m$ phase evolves into the $Fm\bar{3}m$ phase. It is clear how the pressure calculated with quantum effects becomes isotropic when the rhombohedral angle becomes 60°, the angle corresponding to a fcc lattice in a rhombohedral description. Also it is evident that the Wyckoff positions of the $R\bar{3}m$ phase evolve clearly into the $Fm\bar{3}m$ Wyckoff positions, which are summarized in Extended Data Table II.

In Extended Data Figure 6 we show the evolution of the diagonal components of the pressure along the three different Cartesian directions for the monoclininc $C2$ when the lattice structure is relaxed with the SSCHA. The starting point is obtained by first performing a SSCHA relaxation of only internal atomic coordinates keeping the lattice parameters that yield an isotropic stress of 150 GPa. It is clear that quantum effects create an anisotropic stress if the lattice parameters are not modified. When the quantum relaxation of the lattice is performed, the lattice parameters are modified and an isotropic stress is

recovered.

Extended Data Figure 7 shows the structures of the $R\bar{3}m$ and $C2$ phases obtained classically and after the quantum SSCHA relaxation. After the quantum relaxation, the symmetry of both structures is recognized as $Fm\bar{3}m$ with a tolerance of 0.001 Å for lattice vectors and 0.005 Å for ionic positions, consistent with the stochastic accuracy of the SSCHA. In the same Figure 7, the electronic density of states (DOS) as a function of pressure is plotted. Highly symmetric motif ($Fm\bar{3}m$) maximizes N_{E_F}, while in distorted structures ($R\bar{3}m$ and $C2$) the occupation at the Fermi level is reduced by more than 20 %. This underlines that the classical distortions would lower N_{E_F}, reducing λ, as expected in a system destabilized by the electron-phonon interaction.

Transition temperatures from other La-H compositions. Different compositions on the La-H phase diagram have been reported as thermodynamically stable. Presumably, the stabilization of these compositions and the measurement of different T_c's (see Drozdov et al. [5]) demonstrate that other stoichiometries are responsible for these measured T_cs. Notably, these T_cs appear substantially lower, for instance the values decrease from 250 K, to 215 K, 110 K and to 70 K. Experimentally there is not a clear correlation between sample preparation, T_c and pressure. In the sample preparation of Drozdov et al. pressures can vary from 100 to 200 GPa (gradient inside the diamond anvil cell) and it was proposed that other stoichiometries (low-hydrogen content) are responsible for systematically lower T_c's.

Conversely, in a later publication the same authors suggested other hydrogen rich system that is enthalpically competitive (LaH_{11}) is possibly responsible for other high-T_c phases. In order to verify this hypothesis, we did consider structure prediction runs with this stoichiometry and found crystalline structures that were previously reported in Ref. [3]. Extended Data Figure 8 shows the structural motif and the corresponding phonons and $\alpha^2 F(\omega)$ spectral function. We can rule out the possibility that high-T_c, as measured in different samples, arises from LaH_{11} in its $P4/nmm$ (129) structure (lowest enthalpy structure for this composition at relevant experimental pressures). As seen in Extended Data Figure 8, this phase has a strong molecular crystal character, composed of H_2 units weakly interacting with La-lattice. This phase is indeed a poor metal with low occupation of electrons at the Fermi level due to its molecular character and cannot explain 70 K, or higher values of T_c. Our estimated T_c with Allen-Dynes formula, harmonic phonons and using a μ^*=0.1 is 7 K at 100 GPa and reaching $\sim$24 K at 200 GPa. More importantly this phase do not show marked anharmonicity.

DATA AVAILABILITY

All the data generated in this work is available upon request to I.E. and J.A.F.-L.

CODE AVAILABILITY

Quantum ESPRESSO is an open-source suite of computational tools available at www.quantum-espresso.org. VASP is a proprietary program. The SSCHA code is a private code of some of the authors that is in preparation to be distributed as an open-source code.

—————

[31] John P. Perdew, Kieron Burke, and Matthias Ernzerhof. Generalized gradient approximation made simple. *Phys. Rev. Lett.* **77**, 3865 (1996).

[32] Stefano Baroni, Stefano de Gironcoli, Andrea Dal Corso, and Paolo Giannozzi. Phonons and related crystal properties from density-functional perturbation theory. *Rev. Mod. Phys.* **73**, 515 (2001).

[33] Paolo Giannozzi, Stefano Baroni, Nicola Bonini, Matteo Calandra, Roberto Car, Carlo Cavazzoni, Davide Ceresoli, Guido L Chiarotti, Matteo Cococcioni, Ismaila Dabo, Andrea Dal Corso, Stefano de Gironcoli, Stefano Fabris, Guido Fratesi, Ralph Gebauer, Uwe Gerstmann, Christos Gougoussis, Anton Kokalj, Michele Lazzeri, Layla Martin-Samos, Nicola Marzari, Francesco Mauri, Riccardo Mazzarello, Stefano Paolini, Alfredo Pasquarello, Lorenzo Paulatto, Carlo Sbraccia, Sandro Scandolo, Gabriele Sclauzero, Ari P Seitsonen, Alexander Smogunov, Paolo Umari, and Renata M Wentzcovitch. Quantum espresso: a modular and open-source software project for quantum simulations of materials. *Journal of Physics: Condensed Matter* **21**, 395502 (2009).

[34] P Giannozzi, Oliviero Andreussi, T Brumme, O Bunau, M Buongiorno Nardelli, M Calandra, R Car, C Cavazzoni, D Ceresoli, M Cococcioni, et al. Advanced capabilities for materials modelling with quantum espresso. *Journal of Physics: Condensed Matter* **29**, 465901 (2017).

[35] Ion Errea, Matteo Calandra, and Francesco Mauri. First-principles theory of anharmonicity and the inverse isotope effect in superconducting palladium-hydride compounds. *Phys. Rev. Lett.* **111**, 177002 (2013).

[36] Ion Errea, Matteo Calandra, and Francesco Mauri. Anharmonic free energies and phonon dispersions from the stochastic self-consistent harmonic approximation: Application to platinum and palladium hydrides. *Phys. Rev. B* **89**, 064302 (2014).

[37] M. Amsler and S. Goedecker. Crystal structure prediction using the minima hopping method. *The Journal of Chemical Physics* **133**, 224104 (2010).

[38] A. José Flores-Livas, Antonio Sanna, and E.K.U. Gross. High temperature superconductivity in sulfur and selenium hydrides at high pressure. *Eur. Phys. J. B* **89**, 63 (2016).

[39] José A. Flores-Livas, Maximilian Amsler, Christoph Heil, Antonio Sanna, Lilia Boeri, Gianni Profeta, Chris Wolverton, Stefan Goedecker, and E. K. U. Gross. Superconductivity in metastable phases of phosphorus-hydride compounds under high pressure. *Phys. Rev. B* **93**, 020508 (2016).

[40] José A. Flores-Livas, Antonio Sanna, Alexander P. Drozdov, L. Boeri, A. Ganni, Mikhail Eremets, and Stefan Goedecker. Interplay between structure and superconductivity: Metastable phases of phosphorus under pressure *Phys. Rev. Materials* **1**, 024802 (2017).

[41] G. Kresse and J. Furthmüller. Efficiency of ab-initio total energy calculations for metals and semiconductors using a plane-wave basis set. *Comput. Mat. Sci.* **6**, 15-50 (1996).

[42] L. N. Oliveira, E. K. U. Gross, and W. Kohn. Density-functional theory for superconductors. *Phys. Rev. Lett.* **60**, 2430 (1988).

[43] M. Lüders, M. A. L. Marques, N. N. Lathiotakis, A. Floris, G. Profeta, L. Fast, A. Continenza, S. Massidda, and E. K. U. Gross. Ab-initio theory of superconductivity. i. density functional formalism and approximate functionals. *Phys. Rev. B* **72**, 024545 (2005).

[44] José A. Flores-Livas and Antonio Sanna. Superconductivity in intercalated group-iv honeycomb structures. *Phys. Rev. B* **91**, 054508 (2015).

[45] Camilla Pellegrini, Henning Glawe, Antonio Sanna. Density functional theory of superconductivity in doped tungsten oxides. *Phys. Rev. Materials* **3**, 064804 (2019).

[46] M. A. L. Marques, M. Lüders, N. N. Lathiotakis, G. Profeta, A. Floris, L. Fast, A. Continenza, E. K. U. Gross, and S. Massida. Ab initio theory of superconductivity. II. Application to elemental metals. *Phys. Rev. B* **72**, 024546 (2005).

[47] A. Linscheid, A. Sanna, A. Floris, and E. K. U. Gross. First-principles calculation of the real-space order parameter and condensation energy density in phonon-mediated superconductors. *Phys. Rev. Lett.* **115**, 097002 (2015).

[48] S. Massidda, F. Bernardini, C. Bersier, A. Continenza, P. Cudazzo, A. Floris, H. Glawe, M. Monni, S. Pittalis, G. Profeta, A. Sanna, S. Sharma, and E. K. U. Gross. The role of coulomb interaction in the superconducting properties of CaC6 and H under pressure. *Superconductor Science and Technology* **22**, 034006 (2009).

[49] Antonio Sanna, José A. Flores-Livas, Arkadiy Davydov, Gianni Profeta, Kay Dewhurst, Sangeeta Sharma, and E. K. U. Gross. Ab initio Eliashberg Theory: Making Genuine Predictions of Superconducting Features. *J. Phys. Soc. Jpn.* **87**, 041012 (2018).

[50] W. Sano, T. Koretsune, T. Tadano, R. Akashi, and R. Arita. Effect of Van Hove singularities on high-T_c superconductivity in H_3S. *Phys. Rev. B* **93**, 094525 (2016).
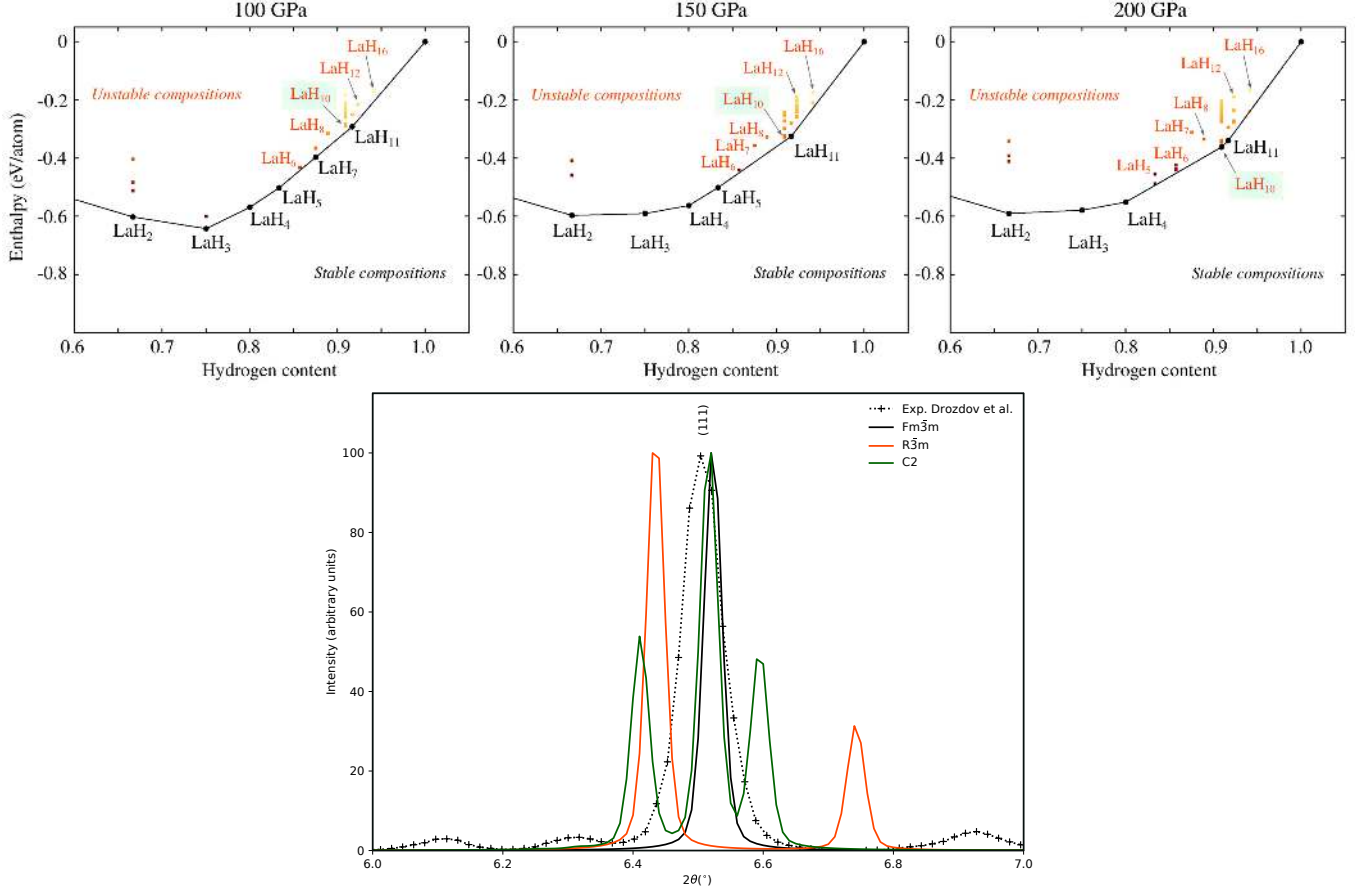
Extended Data Figure 1. Convex hull of enthalpy formation and diffraction pattern of candidate LaH$_{10}$ phases. (Top panels) Classical 200 GPa. At low pressure (100 GPa) the composition of LaH$_{10}$ is not stable and only develops as stable point in the convex convex hull of enthalpy formation for La-H compositions at pressures of 100, 150 an hull above ∼175 GPa. (Bottom panel) Diffraction pattern of different structures at 150 GPa (classical pressure), compared to the experimental data reported by Drozdov et al. in Ref. [5] for $Fm\bar{3}m$ LaH$_{10}$ at 150 GPa. The pattern is shown in the vicinity of the (111) peak of the $Fm\bar{3}m$ phase. This peak is clearly split in the distorted $C2$ and $R\bar{3}m$ phases predicted classically. The figure confirms evidences that the actual experimental resolution in Ref. [5] would have been enough to distinguish between these phases.

Extended Data Table I. Summary of calculated superconducting T$_c$. Values are within different approaches ranging from empirical to fully *ab initio*: McMillan equation (T$_{c\,\mu^*=0.1}^{Mc}$), Allen-Dynes modified McMillan equation (T$_{c\,\mu^*=0.1}^{AD}$), anisotropic treatment of Migdal-Éliashberg (T$_{c\,ani}^{ME}$) and SCDFT (T$_c^{SCDFT}$). Values of λ and ω_{log} are also given.

System	Pressure (GPa)	λ	ω_{log} (meV)	T$_{c\,\mu^*=0.1}^{Mc}$ (K)	T$_{c\,\mu^*=0.1}^{AD}$ (K)	T$_{c\,ani}^{ME}$ (K)	T$_c^{SCDFT}$ (K)
LaH$_{10}$	129	3.62	76.4	171.8	252.6	255.3	230
LaH$_{10}$	163	2.67	96.4	190.4	247.0	242.8	225
LaH$_{10}$	214	2.06	115.5	196.3	235.9	237.9	210
LaH$_{10}$	264	1.73	126.6	189.5	219.2	216.9	201
LaD$_{10}$	159	3.14	63.5	135.0	184.2	180.4	171
LaD$_{10}$	210	2.21	81.7	145.5	176.5	172.9	158
LaD$_{10}$	260	1.80	92.2	142.2	164.6	157.9	151
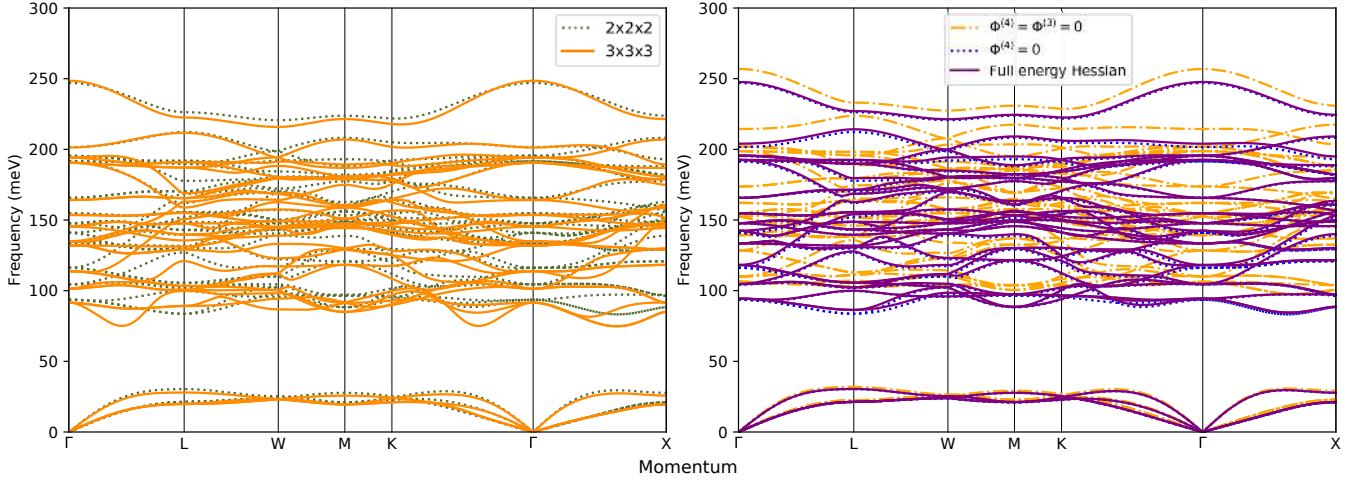
Extended Data Figure 2. **SSCHA phonons supercell convergence and different anharmonic phonon calculations for LaH$_{10}$ at 163 GPa.** (Left panel) The phonon spectra shown are calculated by directly Fourier interpolating the force constants obtained from the Hessian of $E(\mathcal{R})$ in a real space $2 \times 2 \times 2$ and a $3 \times 3 \times 3$ supercell. The similarity of both phonon spectrum obtained by Fourier interpolation indicates that these SSCHA force constants are short-ranged and can be Fourier interpolated. (Right panel) Phonon spectra obtained from the SSCHA energy Hessian of Eq. (1) making different level of approximations. The purple solid line is the phonon spectrum calculated with the full energy Hessian, without any approximation. In the blue dotted spectrum we set $\overset{(4)}{\mathbf{\Phi}} = 0$ in the equation. In the orange dash-dotted line we set $\overset{(3)}{\mathbf{\Phi}} = \overset{(4)}{\mathbf{\Phi}} = 0$, so that the phonon spectra corresponds to the one coming directly from the SSCHA variational force constants $\mathbf{\Phi}$. These results clearly show that while the effect of $\overset{(3)}{\mathbf{\Phi}}$ is important, setting $\overset{(4)}{\mathbf{\Phi}} = 0$ is perfectly safe. All these phonon spectra in the figures are obtained by Fourier interpolating directly the real space anharmonic force constants in a $2 \times 2 \times 2$ supercell.
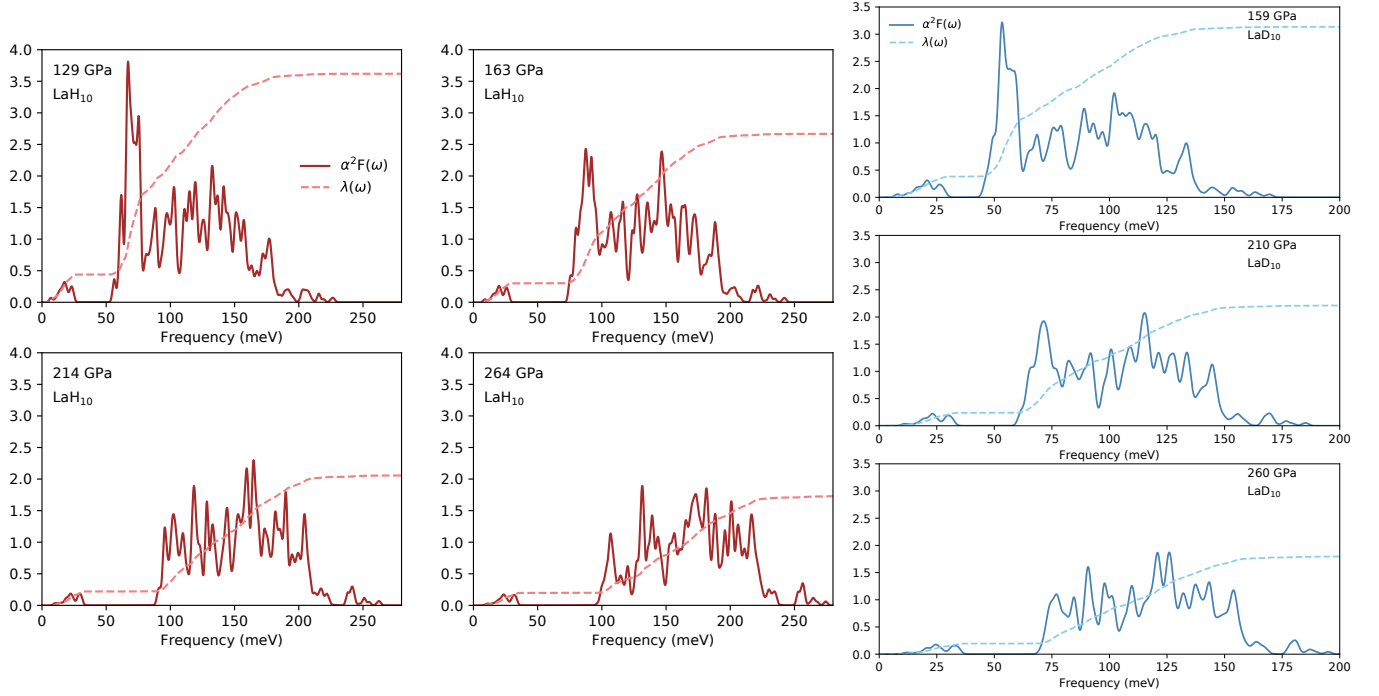
Extended Data Figure 3. $\alpha^2 F(\omega)$ **for the** $Fm\bar{3}m$ **phase of LaH**$_{10}$ **and LaD**$_{10}$. Calculated $\alpha^2 F(\omega)$ for different pressures together with the integrated electron-phonon coupling constant, which is defined as $\lambda(\omega) = 2 \int_0^\omega d\Omega \alpha^2 F(\Omega)/\Omega$. The results show that high frequency, optical modes of hydrogen are responsible for the large value of the electron-phonon coupling constant λ. It is worth noting that acoustic modes with La character contribute between 0.2 and 0.5 to λ and cannot be neglected to estimate an accurate value of T_c.
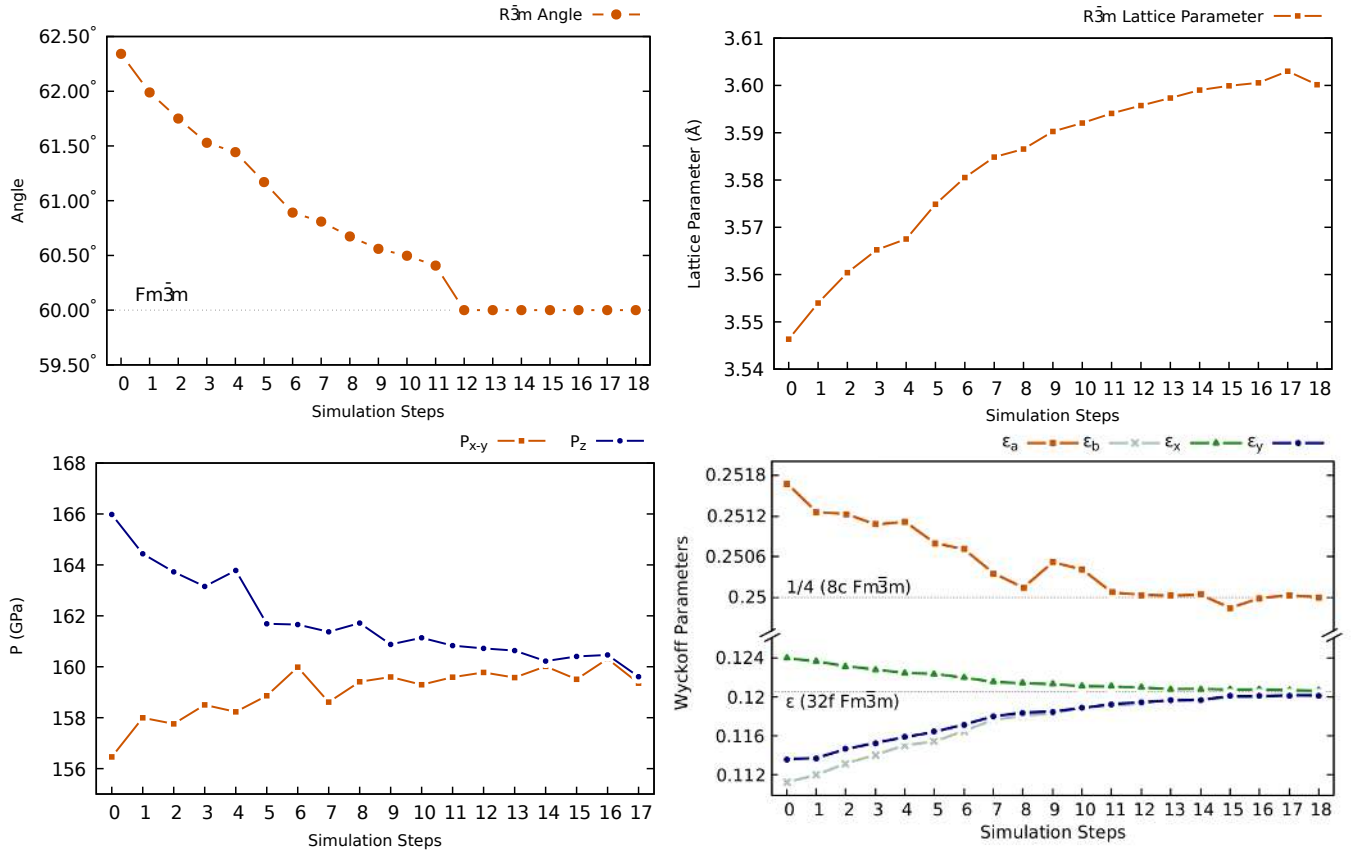
Extended Data Figure 4. **Details on the $R\bar{3}m$ LaH$_{10}$ cell relaxation including quantum effects.** The initial point for the relaxation is the output from the previous internal relaxation with fixed angle presented in Extended Figure 5. The $R\bar{3}m$ phase in the rhombohedral description is described by three vectors of the same length ($a = b = c$) and by the angle between them ($\alpha = \beta = \gamma$). Top left panel shows the evolution of the rhombohedral angle and top left panel shows the evolution of the rhombohedral lattice parameter ($|\mathbf{a}| = |\mathbf{b}| = |\mathbf{c}|$). The progression of the stress tensor in the quantum SSCHA minimization is shown in bottom left panel. It is clear that in the end of the minimization the structure obtains a 60° angle, which matches the angle of a fcc lattice and that in this case the stress is isotropic. In bottom right panel, we show the evolution of the Wyckoff positions in the minimization and we compare it with those of the $Fm\bar{3}m$. The occupied Wyckoff positions for both $R\bar{3}m$ LaH$_{10}$ and $Fm\bar{3}m$ LaH$_{10}$ are summarized in the Extended Data Table II. Here, it can be seen the evolution of ϵ_a, ϵ_b, ϵ_x, and ϵ_y parameters in the minimization. The atoms in the first set of $6c$ positions approach the $8c$ Wyckoff site of the $Fm\bar{3}m$, while the atoms in the second set of $6c$ positions and those in $18h$ sites approach the atoms in the $32f$ Wyckoff site of the $Fm\bar{3}m$, where $\epsilon = 0.12053$.

Extended Data Table II. **Details of the crystal structures.** The table summarizes the occupied Wyckoff positions for different structures found with MHM and used used in SSCHA for minimization. We describe the Wyckoff positions in crystal coordinates so that the $[x, y, z]$ coordinate should be understood as a $x\mathbf{a} + y\mathbf{b} + z\mathbf{c}$ atomic position with $\mathbf{a}$, $\mathbf{b}$, $\mathbf{c}$ the lattice vectors. For the $R\bar{3}m$ phase we use the rhombohedral lattice (R), where the three lattice vectors have the same length ($a = b = c$) and the angle between them is the same ($\alpha = \beta = \gamma$). The $Fm\bar{3}m$ phase is described both in this rhombohedral description (R) and for comparison, in the standard cubic conventional lattice (C). In the $Fm\bar{3}m$ the lanthanum atom is described by the **4b** sites, two hydrogen atoms occupy the **8c** sites, and the remaining 8 hydrogen atoms occupy the **32f** sites. Most of the atomic positions are fixed by symmetry and overall the $Fm\bar{3}m$ structure can be described by one single free parameter (ϵ). In the $R\bar{3}m$ the lanthanum atom is locked in the **3b** sites, two pairs of hydrogen atoms occupy the **6c** sites and the remaining 6 hydrogen atoms occupy the **18h** sites. In this case symmetry allows for more freedom and overall the structure of the $R\bar{3}m$ phase can be described by 4 free parameters (ϵ_a, ϵ_b, ϵ_x and ϵ_y). (b) Lattice parameters and atomic coordinates for LaH_{10} ($Immm$) and LaH_{10} ($C2$) at 150 GPa and LaH_{11} $P4/nmm$ at 100 GPa. These pressures are estimated classically. The positions below give vanishing forces at classical level.

$Fm\bar{3}m$ (C)	$Fm\bar{3}m$ (R)	$R\bar{3}m$ (R)
1 La **4b** $\left[\frac{1}{2},\frac{1}{2},\frac{1}{2}\right]$	1 La **4b** $\left[\frac{1}{2},\frac{1}{2},\frac{1}{2}\right]$	1 La **3b** $\left[\frac{1}{2},\frac{1}{2},\frac{1}{2}\right]$
2 H **8c** $\left[\frac{1}{4},\frac{1}{4},\frac{1}{4}\right]$ $\left[\frac{3}{4},\frac{3}{4},\frac{3}{4}\right]$	2 H **8c** $\left[\frac{1}{4},\frac{1}{4},\frac{1}{4}\right]$ $\left[\frac{3}{4},\frac{3}{4},\frac{3}{4}\right]$	2 H **6c** $[\epsilon_a,\epsilon_a,\epsilon_a]$ $[-\epsilon_a,-\epsilon_a,-\epsilon_a]$
8 H **32f** $[\epsilon,\epsilon,\epsilon]$ $[-\epsilon,-\epsilon,-\epsilon]$ $[\epsilon,\epsilon,-\epsilon]$ $[\epsilon,-\epsilon,\epsilon]$ $[-\epsilon,\epsilon,\epsilon]$ $[-\epsilon,-\epsilon,\epsilon]$ $[-\epsilon,\epsilon,-\epsilon]$ $[\epsilon,-\epsilon,-\epsilon]$	8 H **32f** $[\epsilon,\epsilon,\epsilon]$ $[-\epsilon,-\epsilon,-\epsilon]$ $[-\epsilon,-\epsilon,3\epsilon]$ $[-\epsilon,3\epsilon,-\epsilon]$ $[3\epsilon,-\epsilon,-\epsilon]$ $[\epsilon,\epsilon,-3\epsilon]$ $[\epsilon,-3\epsilon,\epsilon]$ $[-3\epsilon,\epsilon,\epsilon]$	2 H **6c** $[\epsilon_b,\epsilon_b,\epsilon_b]$ $[-\epsilon_b,-\epsilon_b,-\epsilon_b]$ 6 H **18h** $[-\epsilon_x,-\epsilon_x,3\epsilon_y]$ $[-\epsilon_y,3\epsilon_x,-\epsilon_x]$ $[3\epsilon_y,-\epsilon_x,-\epsilon_x]$ $[\epsilon_x,\epsilon_x,-3\epsilon_y]$ $[\epsilon_x,-3\epsilon_y,\epsilon_x]$ $[-3\epsilon_y,\epsilon_x,\epsilon_x]$

| Composition (Space group)	Lattice parameters	Wyckoff positions	
LaH_{10} ($Immm$)	$a = 3.58303$ Å	La **2c**	[0.50000, 0.50000, 0.00000]
	$b = 3.61834$ Å	H **8m**	[0.75841, 0.00000, 0.11649]
	$c = 5.08749$ Å	H **8l**	[0.00000, 0.75742, 0.87548]
		H **4j**	[0.50000, 0.00000, 0.74572]
LaH_{10} ($C2$)	$a = 6.15468$ Å	La **4c**	[0.49244, 0.00070, 0.25292]
	$b = 3.60628$ Å	H **4c**	[0.13978, 0.24567, -0.05243]
	$c = 7.23776$ Å	H **4c**	[0.09798, 0.24122, 0.45027]
	$\beta = 55.71434°$	H **4c**	[0.36015, 0.25590, 0.05238]
		H **4c**	[0.40204, 0.26021, 0.54971]
		H **4c**	[-0.09751, 0.00051, -0.05100]
		H **4c**	[0.86810, 0.00071, 0.43706]
		H **4c**	[0.88713, 0.00076, 0.69398]
		H **4c**	[0.87083, 0.00068, 0.19089]
		H **4c**	[0.73058, 0.00043, 0.88088]
		H **4c**	[0.76156, 0.00071, 0.36763]
LaH_{11} ($P4/nmm$)	$a = 3.87435$ Å	La **2c**	[0.25000, 0.25000, 0.78577]
	$b = 3.87435$ Å	H **4e**	[0.00000, 0.00000, 0.50000]
	$c = 5.27636$ Å	H **8i**	[0.25000, -0.02052, 0.17824]
		H **8i**	[0.25000, 0.55418, 0.35160]
		H **2a**	[0.75000, 0.25000, 0.00000]
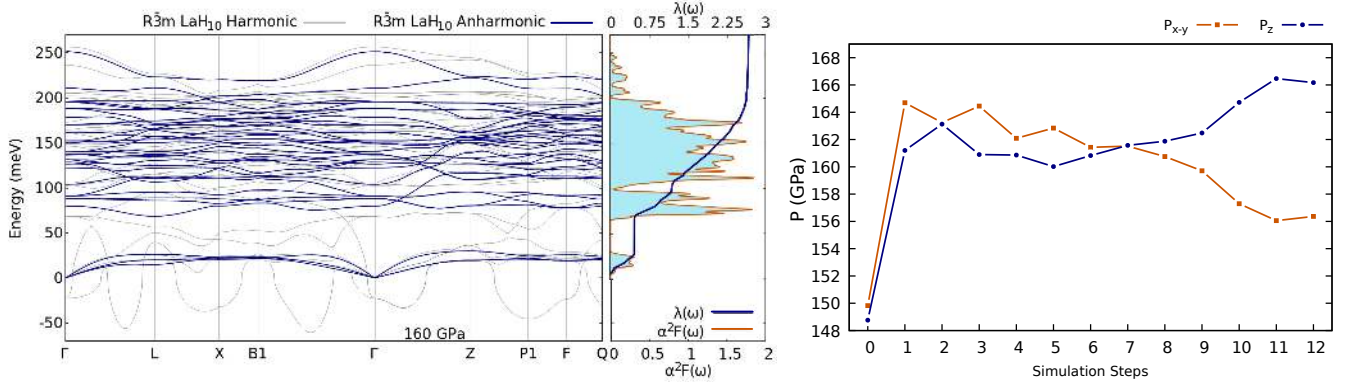
Extended Data Figure 5. **Phonon dispersion of $R\bar{3}m$ LaH$_{10}$ and the anisotropic pressure created in a fixed-cell quantum relaxation.** (Left panel) Harmonic and anharmonic phonon spectrum keeping a 62.3° rhombohedral angle. The harmonic calculation is performed with the internal atomic positions that yield classical vanishing forces. The anharmonic calculation is performed after relaxing with the SSCHA the internal degrees of freedom but keeping the 62.3° rhombohedral angle. At the harmonic level there are unstable phonon modes even at Γ. Symmetry prevents the relaxation of this structure according to the unstable phonon mode at Γ. The harmonic phonons are calculated at a classic pressure of 150 GPa. Quantum effects add an extra $\sim$10 GPa to the pressure. On the right side of the figure is also shown the behavior of $\lambda(\omega)$ and $\alpha^2 F(\omega)$ for the anharmonic calculation. (Right panel) Pressure along the different Cartesian directions during the SSCHA relaxation of the internal parameters keeping the rhombohedral angle at 62.3° fixed. At step 0 the pressure reported is obtained directly from $V(\mathbf{R})$, neglecting quantum effects. It is isotropic within one GPa of difference between the $x - y$ and z directions. At the other steps it is calculated from the quantum $E(\mathcal{R})$ and along the minimization it becomes anisotropic. When the minimization stops at step 12, i.e., the internal coordinates are at the minimum of the $E(\mathcal{R})$ for this lattice, the stress anisotropy between z and $x - y$ directions is about 6%. This clearly indicates that quantum effects want to relax the crystal lattice, in particular, since P_z is larger, by reducing the rhombohedral angle. It is worth noting that quantum effects approximately increase the total pressure by 10 GPa, which is calculated as $P = (P_x + P_y + P_z)/3$. The initial cell parameters before the minimization are $a = 3.5473398$ Å and $\alpha = 62.34158$ °. The initial values of the free Wyckoff parameters, which yield classical vanishing forces and a 150 GPa isotropic stress, are $\epsilon_a = 0.26043$, $\epsilon_b = 0.09950$, $\epsilon_x = 0.10746$ and $\epsilon_y = 0.12810$. See Extended Data Table II for more details.
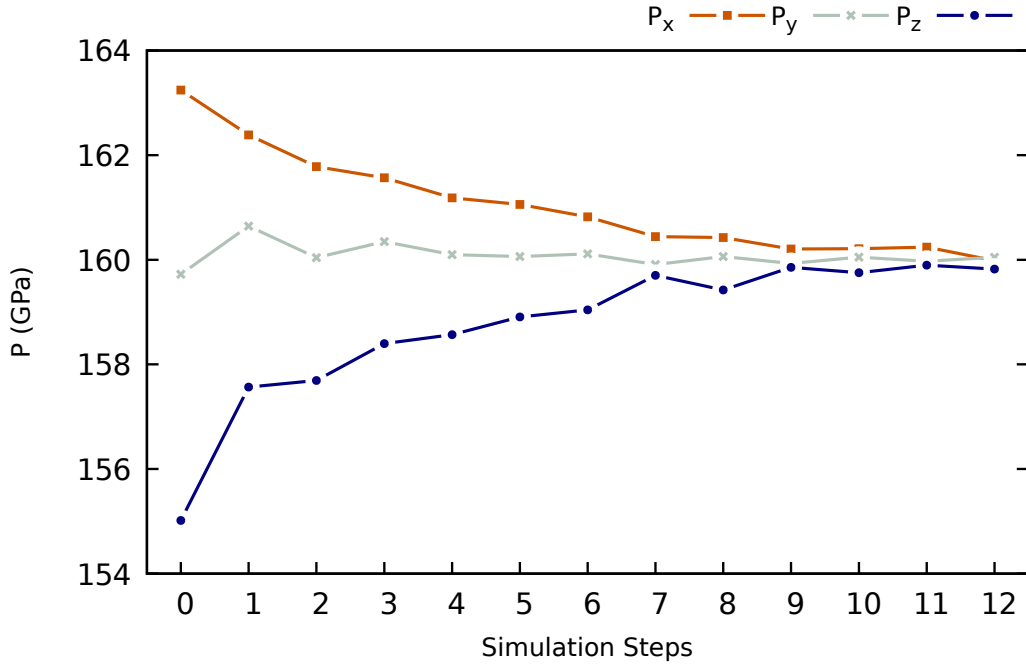
Extended Data Figure 6. **Anisotropic pressure of the $C2$ phase of LaH$_{10}$ in a cell quantum relaxation.** The figure shows the pressures along the different Cartesian directions during the SSCHA cell minimization. The target pressure for this minimization is 160 GPa. At the end of the minimization the isotropy of the stress tensor is recovered. A symmetry analysis performed on the structure at the end of the minimization confirms the $C2$ LaH$_{10}$ evolves in the $Fm\overline{3}m$ LaH$_{10}$. The initial values $P_x = 163.2$ (GPa), $P_y = 159.7$(GPa), $P_z = 155.0$(GPa) are obtained by an atomic internal relaxation performed using the SSCHA with fixed cell.
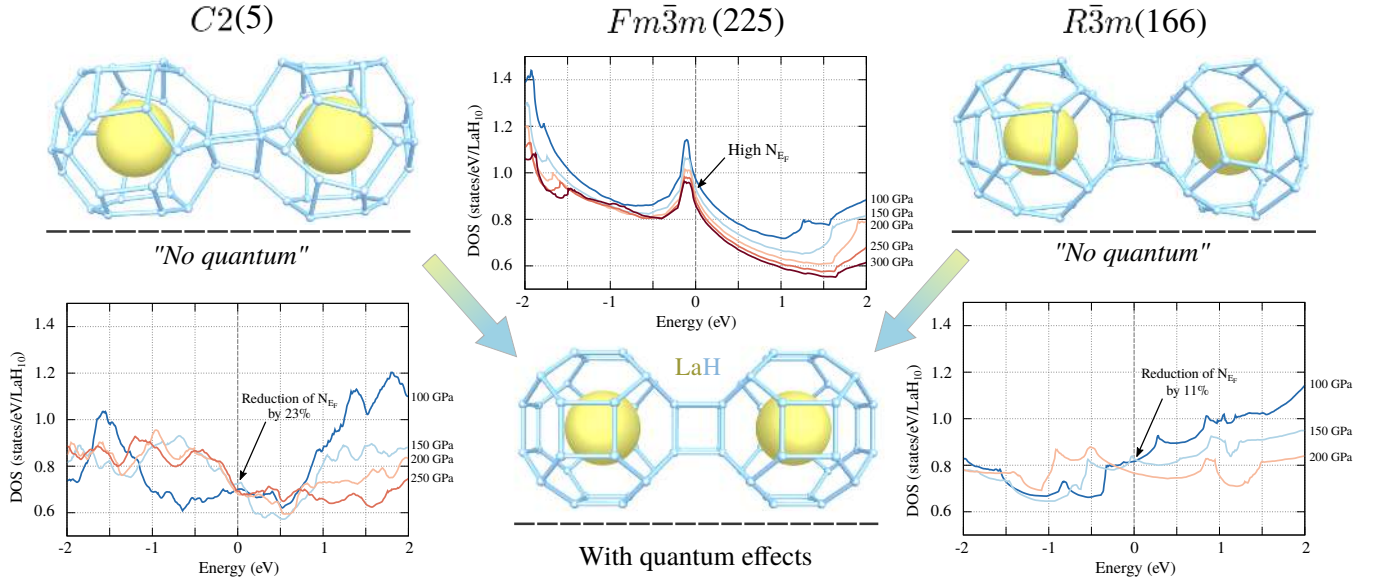
Extended Data Figure 7. **SSCHA minimization on LaH$_{10}$ and DOS.** Top figures: two initial structures ($C2$ and $R\bar{3}m$) low enthalpy, considered in our SSCHA simulations. When considering quantum effects both structures evolve towards the $Fm\bar{3}m$ structure. Corresponding total electronic density of states (DOS) as a function of pressure are plotted for each structure (for comparison in the same energy scale). Highly symmetric motif ($Fm\bar{3}m$) maximizes N_{E_F}, while in distorted structures ($R\bar{3}m$ and $C2$) the occupation at the Fermi level is reduced by more than 23 % for $C2$ and by 11 % for $R\bar{3}m$, both comparison at 150 GPa w.r.t. $Fm\bar{3}m$. Classical pressures are appended for comparison in DOS panels. Note that DOS shape is also strongly modified.
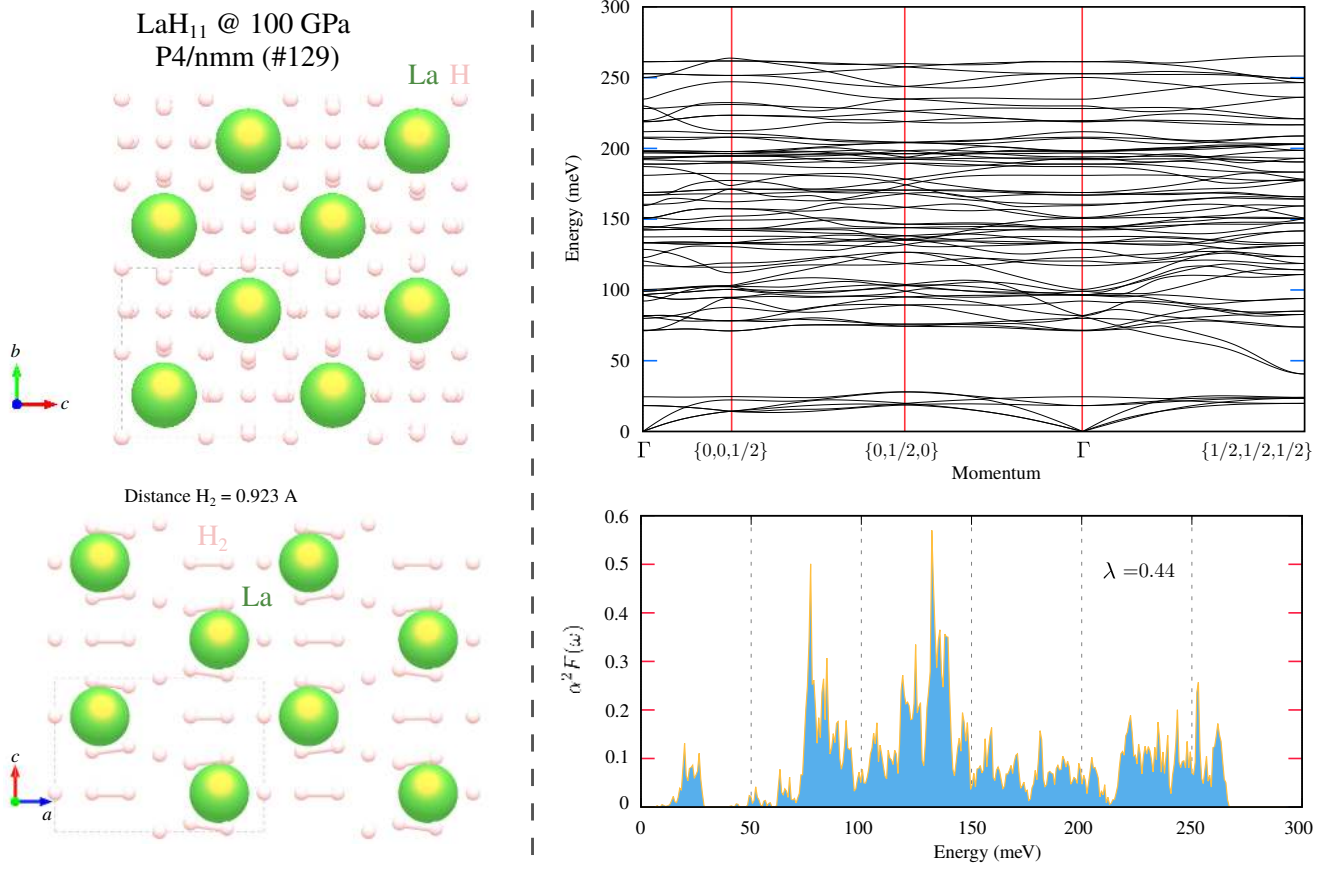
Extended Data Figure 8. **Details on LaH$_{11}$.** Left: $P4/nmm$ crystal structure of LaH$_{11}$ at 100 GPa thermodynamically stable in the convex hull. Right top: harmonic phonons dispersion along momentum space for this composition: it is dynamically stable. Right bottom: superconducting Éliashberg spectrum function ($\alpha^2 F(\omega)$) calculated for this composition at the pressure indicated with harmonic phonons. The estimated T$_c$ with Allen-Dynes formula (μ^*=0.1) is $\sim$7 K at 100 GPa (harmonic phonons).